Enhanced Mechanical Properties and Corrosion Behavior of Biodegradable Mg-Zn/HA Composite

EMEE MARINA SALLEH, HUSSAIN ZUHAILAWATI, SIVAKUMAR RAMAKRISHNAN, and BRIJ KUMAR DHINDAW

Magnesium (Mg) and its alloys have shown potential for use in the biomedical industry due to their excellent biological performance and biodegradability in the bioenvironment. Thus, the aim of the present study was to develop a reliable biodegradable hard tissue substituent. Biodegradable and bioactive Mg-Zinc (Zn) reinforced by hydroxyapatite (HA) composite was prepared using mechanically alloyed Mg-6.5 wt pct Zn and pure HA powders as starting materials. Various HA contents (*i.e.*, 5, 10, 15, and 20 wt pct) were introduced in forming the Mg-Zn/HA composite. The effect of bioactive HA incorporation in biodegradable Mg-6.5 wt pct Zn alloy matrix on mechanical and biodegradation properties as well as microstructural observation was investigated. As measured by the Williamson–Hall formula, the Mg crystallite size of the sintered composites containing 5, 10, 15, and 20 wt pct HA were 36.76, 29.08, 27.93, and 27.31 nm, respectively. According to X-ray diffraction (XRD) analysis, there was no new crystalline phase formed during milling, indicating that no mechanochemical reactions between Mg-Zn alloy and HA occurred. The −1.70 V shifted significantly toward the passive position of the plain Mg-6.5 wt pct Zn alloy and Mg-Zn/10 wt pct HA composite, which were −1.50 and −1.46 V, respectively, indicating that the Mg-Zn/10 wt pct HA composite was least susceptible to corrosion in the bioenvironment.

DOI: 10.1007/s11661-017-4028-7
© The Minerals, Metals & Materials Society and ASM International 2017

I. INTRODUCTION

MAGNESIUM (Mg) alloys have attracted considerable attention for biomaterial applications due to their low density, inherent biocompatibility, and resemblance of mechanical properties to human bone. Magnesium is able to degrade and to be safely absorbed in the physiological media, and excess Mg can be efficiently filtered by the kidneys.[1,2] To date, a number of approaches have been developed to produce biodegradable Mg alloy with adjustable *in vitro* and *in vivo* corrosion rates, while the mechanical integrity is not compromised. Another important point for a biomaterial is the ability of the implant to establish bonding with the surrounding bone tissue, which is bioactivity of the implant.[3,4] Therefore, it seems necessary to increase the bioactivity of Mg-based materials. An approach to this challenge might be the application of metal matrix composite (MMC). The advantage of using MMCs as biomaterials is the adjustable mechanical properties (Young's modulus and compressive and tensile strength) as well as the adjustable corrosion behavior by choosing suitable reinforcement materials. Introducing bioactive particles containing Ca is known to reduce the susceptibility of Mg to corrode when added in amounts of a few tenths weight percent.[5,6] As a natural bone composition, bioactive hydroxyapatite (HA; $Ca_{10}(PO_4)_6(OH)_2$) is known to possess a low solubility in body environment. HA seems to be an appropriate reinforcement particle in Mg-based implants, as HA presents a good ability to induce the deposition of Ca-P compounds that can increase the surface biocompatibility and bioactivity of the Mg alloy matrix materials.[7–9]

Witte *et al.*[10] produced MMC made of AZ91D alloy reinforced with 20 wt pct HA powder by mixing the raw powders and subsequent extrusion at 673 K (400 °C) to a diameter of 18 mm. From the study, corrosion tests revealed that HA particles stabilized the corrosion rate and exhibited more uniform corrosion attack in both artificial sea water and cell solutions. Cocultivation of AZ91D-HA revealed that the human bone derived cells; cells of osteoblast lineage and cells of macrophage lineage adhered, proliferated, and survived on the corroding surface of AZ91D-HA composite. However, the presence of aluminum (Al) has been shown to increase estrogen-related gene expression in human breast cancer cells when cultured in a laboratory setting.[2,5] In summary, biodegradable and cytocompatible Al-free Mg-based implants with adjustable mechanical and corrosion properties might be achieved by incorporating bioactive HA particles into the matrix.

EMEE MARINA SALLEH, HUSSAIN ZUHAILAWATI, and SIVAKUMAR RAMAKRISHNAN are with the Biomaterials Niche Area, School of Materials and Mineral Resources Engineering, Engineering Campus, Universiti Sains Malaysia, 14300 Nibong Tebal, Penang, Malaysia. Contact e-mail: zuhaila@usm.my BRIJ KUMAR DHINDAW is with the School of Minerals Metallurgical and Materials Engineering, Indian Institute of Technology, Bhubaneswar, 751007, India.

Manuscript submitted September 1, 2016.
Article published online March 6, 2017

In the present research work, different amounts of HA were incorporated into Mg-6.5 wt pct zinc (Zn) alloy matrix in order to produce HA-reinforced composites. The Mg-Zn/HA composites were fabricated following a powder metallurgy route that included mechanical alloying (for producing alloy matrix) and ball mixing (for producing HA-reinforced composite), which was then uniaxially compacted and sintered. The effect of HA content on the resulting properties of Mg-Zn alloy-based composite was evaluated for both mechanical properties and degradation behavior.

II. EXPERIMENTAL WORK

Mg-6.5 wt pct Zn alloy was used as a metallic matrix in fabricating Mg-Zn/HA composite. A mixture of elemental Mg powder (99.00 pct pure) and Zn powder (99.90 pct pure) was mechanically alloyed at room temperature using a high-energy Fritsch Pulveristte P-5 planetary mill under argon atmosphere. Twenty-millimeter-diameter stainless steel balls were used during mechanical alloying. HA powder of 99.00 pct purity was added into the as-milled biodegradable Mg-6.5 wt pct Zn alloy matrix. Mg-Zn/HA composites with 5, 10, 15, and 20 wt pct HA were fabricated through a powder metallurgy route consisting of low-energy ball mixing of the raw powders and subsequent consolidation. The mechanically milled Mg-Zn/HA powder mixture was loaded into a polyethylene bottle together with several 5-mm-diameter alumina (Al_3O_2) ball mills. The powder milling was run at 100 rpm for 24 hours in order to produce a well-mixed powder mixture. The milled powders were uniaxially cold pressed under 400 MPa for 2 minutes at room temperature to produce 10-mm diameter of green Mg-Zn/HA composite compacts and sintered at 623 K (350 °C) under argon flow at consistent heating and cooling rates of 10 K/min for an hour in order to form solid bodies. Qualitative X-ray diffraction (XRD) analysis with an angular scanning range of 20 deg $\leq 2\theta \leq$ 90 deg was conducted to identify the presence of any element and phase. The data were obtained using a D8 Advance, Bruker AXS. APW software was used to analyze the diffractogram to identify the phase present in the samples. The density of the sintered composite was measured by pycnometer density equipment according to Archimedes' principle. The samples were immersed in tap water that was placed on a Precisa electronic analytical balance with four-decimal accuracy. Ten readings were taken from the sample. Relative density (TD pct) was calculated according to

$$\text{TD pct} = (\text{actual density}/\text{density}_{\text{ROM}}) \times 100 \text{ pct} \quad [1]$$

$$\text{density}_{\text{ROM}} = \rho_{\text{Mg}} V_{\text{Mg}} + \rho_{\text{Zn}} V_{\text{Zn}} \quad [2]$$

$$V_{\text{Mg}} + V_{\text{Zn}} = 1 \quad [3]$$

where ρ_{Mg} and ρ_{Zn} represent the density of Mg and Zn, respectively, and V_{Mg} and V_{Zn} represent the volume fraction of Mg and Zn, respectively, incorporated in the alloy material.[11] The relative density is useful for comparing the measured sintered density to the predicted rule-of-mixtures density. A microhardness test using a LECO tester (LECO Corporation, St. Joseph, MI) was carried out by placing samples of 10-mm diameter under a diamond indenter. The test was performed under 500 gf of indentation load with 10 seconds of dwell time. Ten readings were taken from the same sample.

Mechanical tests were performed according ASTM E9-09 standards for compression testing of metallic materials at room temperature using a universal testing machine. Cylindrical specimens of sintered compacts with dimension 10-mm diameter and length 10 mm were prepared. Compression characteristics were tested at room temperature at a constant crosshead speed and a strain rate of 0.5 mm/min. All mechanical tests were replicated 5 times.

Tafel polarization is the most commonly used electrochemical technique for studying *in vitro* corrosion of metallic implants. A working surface of specimen with 10-mm diameter was ground with SiC emery papers up to 2000 grit. An electrochemical test was conducted at 310 K ± 5 K (37 °C ± 0.5 °C) in an open glass cell containing artificial body fluid using Hank's balanced salt solution (HBSS) on a potentiostat/galvanostat of "automatic laboratory" corrosion measurement system. A standard three-electrode configuration with a saturated calomel electrode as a reference, a platinum electrode as the counter, and the specimen as the working electrode was applied. Five measurements were repeated for each specimen.

III. RESULTS AND DISCUSSION

A. *Characterization of Raw Starting Powders*

Scanning electron microscopy (SEM) micrographs of the starting Mg and Zn powders are shown in Figure 1. Magnesium powders are irregular shaped and Zn powders are mostly ellipsoidal, elongated particles. The average particle sizes of elemental Mg powder and Zn powder are 227.41 and 121.65 μm, respectively, as shown in Table I.

The XRD pattern shows the reflections expected for the starting HA [$Ca_{10}(PO_4)_6(OH)_2$] powder. The unit cell of the synthetic HA phase was hexagonal, and the lattice parameters were a = 9.411 Å and c = 6.759 Å. As shown in Figure 2, the strong peaks of HA were in the range of 2θ = 20 to 55 deg. The SEM observation revealed that the morphology of starting HA powder consisted of agglomeration of fine particles (1.12 to 6.07 μm), and the shape of the powder particles was mainly nonspherical and angular structure.

B. *Phase and Microstructural Analysis*

The XRD diffractogram of sintered Mg-6.5 wt pct Zn/HA composite compacts in Figure 3 indicates the presence of α-Mg and HA phase. There was no oxide or any other phase observed. As can be seen, the diffraction

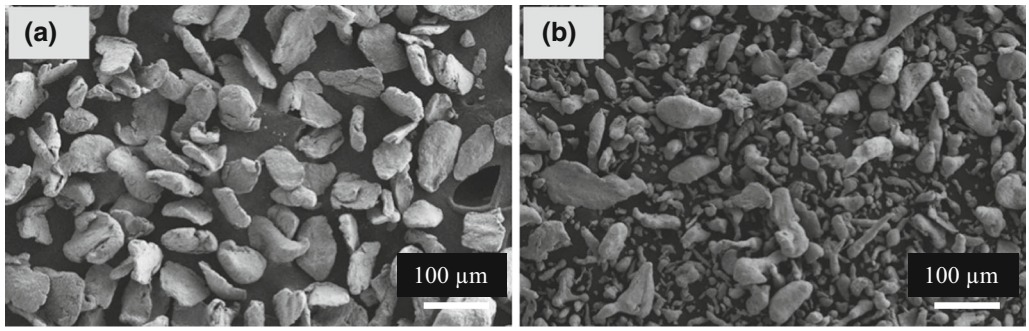

Fig. 1—Micrographs of elemental (*a*) Mg and (*b*) Zn powders.

Table I. Distribution of Average Particle Size of Mg and Zn Powders

Powder	D10 (μm)	D50 (μm)	D90 (μm)
Mg	61.33	102.63	227.41
Zn	27.60	65.81	121.65

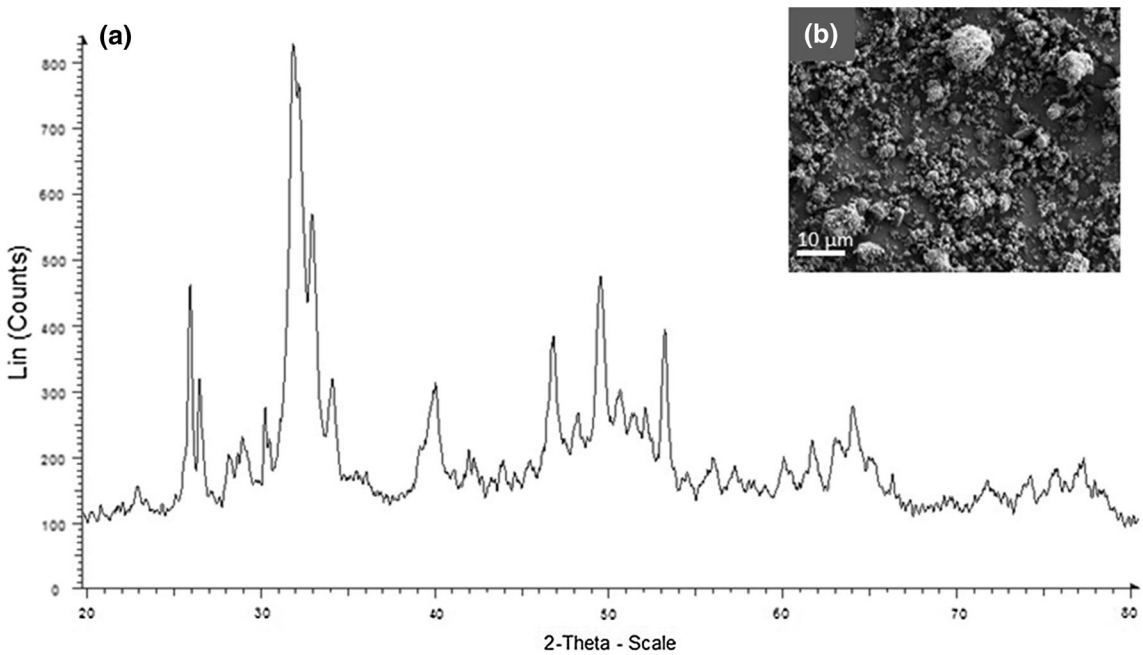

Fig. 2—(*a*) XRD pattern and (*b*) morphology of raw HA powder.

peaks broadened, as explained by the refinement of Mg crystallite.[12] The refinement of Mg crystallite size resulted from the collisions between powders and balls during MA.[13] As measured by the Williamson–Hall formula, the Mg crystallite sizes of the sintered composites containing 5, 10, 15, and 20 wt pct HA were 36.76, 29.08, 27.93, and 27.31 nm, respectively. In addition, diffraction peaks shifted to a lower diffraction and broadened as a function of content, which suggested that the HA powder homogeneously dispersed in the Mg-based alloy matrix. There was no new crystalline phase formed during milling, indicating that no mechanochemical reactions between Mg-Zn alloy and HA occurred.[14]

Figure 4 shows the morphology of sintered compacts and as-milled Mg-6.5 wt pct Zn/HA composite at different additions of HA content. As illustrated, the as-milled powder particles of 5 wt pct HA composite were heterogeneously large in size but relatively smaller compared to the initial unmilled starting powders. The sintered compacts were dispersed by uniform HA powder corresponding to white distribution of particles, as shown in the micrograph. As the HA content was increased to 10 wt pct, the as-milled particles were refined with a more homogenous size. The powder refinement indicated that the hard HA particles started to promote fracturing effect and, thus, resulted in finer particle size with the addition of high impact of repeated

fracturing during MA. The fine particles had high tendency to be uniformly dispersed in the alloy matrix, as shown in the micrographs. Further increase in HA content from 15 to 20 wt pct caused the formation of angular at the large difference in size of as-milled particles, thus resulting in the nonuniform regional dispersion of the HA in the sintered compacts. The nonuniformity of the particle dispersion was suspected to deteriorate the bulk properties of the fabricated composite.[12,13]

C. *Density and Microhardness Measurement*

Table II shows the density and relative density measurements of Mg-6.5 wt pct Zn/HA composite. The results revealed that nearly dense Mg-Zn alloy and composite materials could be attained using the fabrication methodology adopted in this study. The density tended to increase with the HA content, which obeyed the density distribution according to the ROM formula. The theoretical density of Mg-6.5 wt pct Zn alloy is 2.0981 g/cm^3, and the measured density of the composites increased when the higher density HA (3.11 g/cm^3) particles were added into the Mg-Zn alloy matrix as a function of HA content. However, the relative densities of the composites initially increased with increasing HA content up to 10 wt pct but then slightly reduced. As can be seen, the relative density of the sintered composites reached as high as 94.77 pct in the Mg-6.5 wt pct Zn matrix composite containing 10 wt pct HA.

Figure 5 shows the relative density and microhardness of Mg-6.5 wt pct Zn/HA composite as a function of milling time. The microhardness gradually increased as the HA particles were added up to 10 wt pct into the Mg-6.5 wt pct Zn matrix. The microhardness of Mg-Zn alloy incorporated with 5 to 10 wt pct HA increased from 101 to 131 HV, and the relative density reached as high as 94.77 pct. The reason for the increase in relative density and microhardness was due to the existence of HA-fragmented microparticles in the Mg-Zn alloy matrix.

Remarkably, with an increase of more than 10 wt pct HA, the relative density and microhardness were reduced. The reduction of relative density and microhardness of the composites was attributed to two reasons. First, some degree of HA particle clustering took place during MA.[14,15] Second, the sintering temperature of pure HA is above 1273 K (1000 °C).[15,16] When increasing the HA content in the Mg-6.5 wt pct Zn alloy matrix, the sintering temperature of 623 K (350 °C) was considerably insufficient for achieving high densification. Notably, increasing the sintering temperature was not possible due to the low melting temperatures of Mg [923 K (650 °C)] and Zn [693 K (420 °C)] in order to sustain a solid-state processing condition.

D. *Effect of HA Content on Mechanical Property*

Sintered compacts of crystalline Mg-6.5 wt pct Zn alloy and Mg-6.5 wt pct Zn/HA composites were subjected to mechanical testing in order to determine their failure strength under uniaxial compressive loading. As shown in Table III, it was clear that in the sintered compact of plain Mg-Zn alloy containing 0 wt pct HA, the compressive strength was low, about 249 MPa. As the content of HA was increased to 10 wt pct, the compressive strength increased as high as 292 MPa due to enhancement of composite densification. A further increase in HA content (from 15 to 20 wt pct) slightly reduced the compressive strength resulting from the low densification of Mg-6.5 wt pct Zn/HA composite. In addition, the failure strain decreased with increasing HA content. However, at a relatively high HA addition (more than 10 wt pct), the failure strain of the composite expressively reduced. The reduction of strain was the result of the presence of a high volume fraction of hard and brittle HA particles, which thus lowered the intrinsic ductility of Mg-Zn alloy.

E. *Effect of HA Content on Corrosion Behavior*

Table IV summarizes the corresponding electrochemical data derived from the polarization curves. As stated in the table, the changes in the corrosion potential of the Mg-Zn alloy-based composites might be ascribed to the low electronegativity of the bioactive incorporating element added to the alloys. As the results showed, the addition of HA from 0 to 10 wt pct reduced the corrosion current density of the Mg-6.5 wt pct Zn/HA composites from 9.18×10^{-4} to 1.3077×10^{-5} A cm^{-2}. With the same direction, the polarization resistance increase (corrosion rate decrease) might be correlated to the microstructure refinement and densification increment, which was caused by the addition of HA to the alloy matrix. The microstructure refinement created more grain boundaries, where the grain boundaries can act as physical barriers, and the densification increment decreased the size and distribution of pores, thus resulting in reduction of the degradation rate.[17]

However, further addition of HA from 15 to 20 wt pct in the alloy matrix deteriorated the corrosion resistance due to the agglomeration of HA particles. The agglomeration of HA particles was found to degrade the interfacial bonding strength between the matrix and reinforcement, leading to the formation of pores.[18] The pores became potential sites to be initially attacked by the media when the material was exposed to the corrosive environment. A higher amount and larger size of pores resulted in a higher rate of degradation.[14] An increase in HA content increased the corrosion rate of Mg, which could be explained by more anodic sites forming galvanic coupling in the Mg matrix composite due to the high volume fraction of the HA particles.[19] Therefore, the Mg composite with 10 wt pct HA is desirable, since this composite displayed a combination of improved mechanical properties and corrosion behavior.

F. *Compressive Characteristics of Pure Mg, Mg-Zn Alloy, and Mg-Zn/HA Composite*

The compressive stress-strain curves of pure Mg, Mg-6.5 wt pct Zn-0 wt pct HA (denoted as Mg-Zn

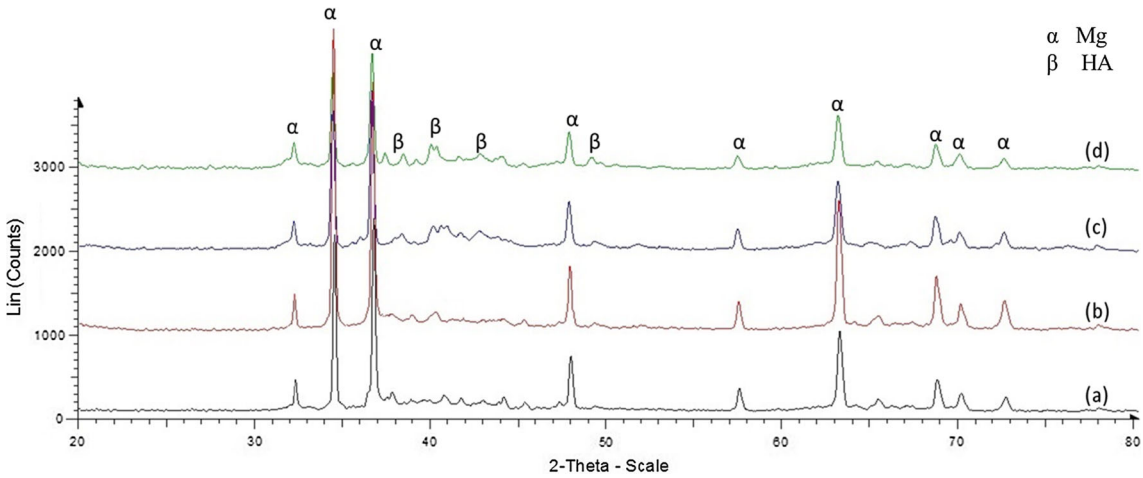

Fig. 3—XRD pattern of Mg-Zn alloy matrix composite for (*a*) 5 wt pct, (*b*) 10 wt pct, (*c*) 15 wt pct, and (*d*) 20 wt pct HA content.

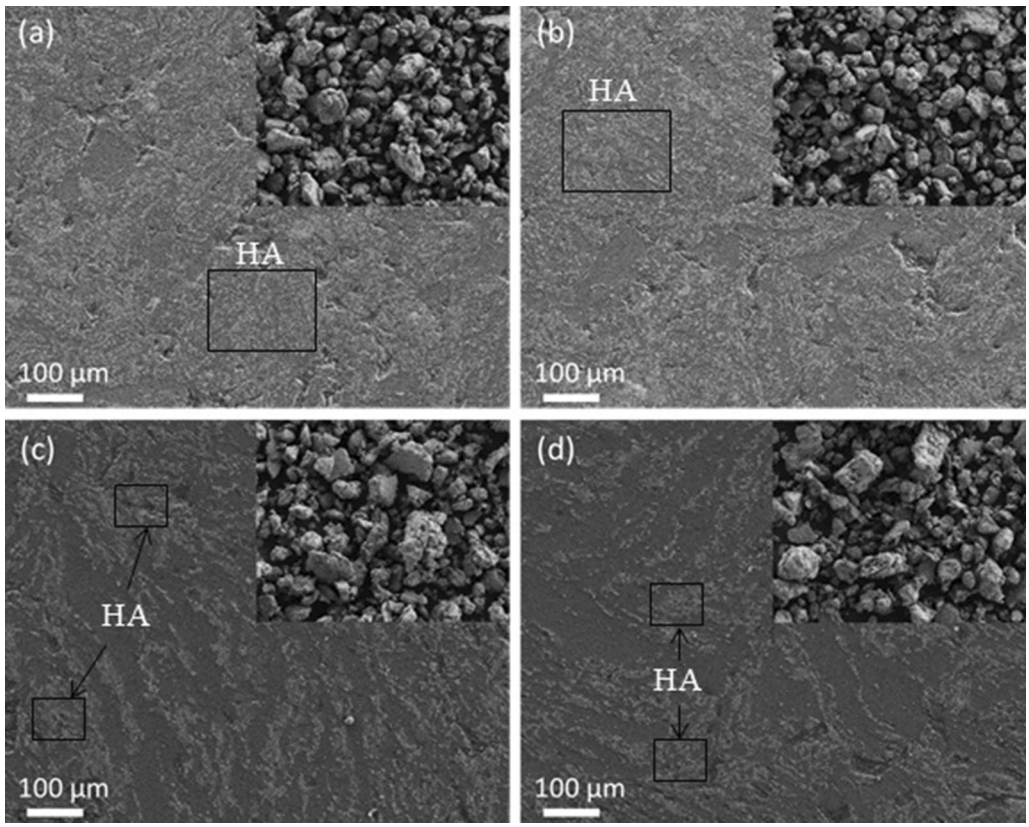

Fig. 4—Morphology of sintered compact and as-milled powder (inserted images) of (*a*) 5 wt pct, (*b*) 10 wt pct, (*c*) 15 wt pct, and (*d*) 20 wt pct HA content.

Table II. Density Profile of Mg-Zn Alloy and Mg-Zn/HA Composite

Mg-6.5Zn (Wt Pct)	HA (Wt Pct)	Theoretical Density (g/cm^3)	Measured Density (g/cm^3)	Relative Density (Pct)
100	0	2.0891	1.9159	91.7093
95	5	2.1401	1.9909	93.0284
90	10	2.1912	2.0765	94.7674
85	15	2.2442	2.0829	92.8935
80	20	2.2933	2.1094	91.9810

alloy), and Mg-6.5 wt pct Zn-10 wt pct HA (denoted as Mg-Zn/HA composite) are graphically presented in Figure 6. S-shaped compressive curves were observed where the curves exhibited moderate and significant hardening parts. As can be seen at low applied stress (less than 50 MPa), there were toe regions in all studied materials. The toe region was due to the initial compaction of pores prior to the applied compression stress. Clearly, the compressive yield strength of pure Mg was 141 MPa, which then improved with the addition of 6.5 wt pct Zn (154 MPa) and showed the highest yield strength (175 MPa) when the alloy was incorporated with 10 wt pct HA. The yield strength is defined as the applied stress at 0.2 pct of plastic deformation. The remarkable feature in the compression curve of pure Mg is a yield diminution once the yield strength was reached and the subsequent gradual increase of the plastic deformation until fracture.[20,21]

Magnesium has a hexagonal-close-packed (hcp) crystal structure and a slightly less than ideal c/a ratio. As can be seen, there was a large plateau stress in the plastic region due to the energy absorption, indicating twinning activity before failure. The dominant slip systems in Mg are the $(0001)\langle 10\bar{2}0\rangle$ basal slip system and the $\{10\bar{1}0\}\langle 11\bar{2}0\rangle$ prismatic slip system.[22] The deformation curves, as obtained in Figure 6, show the typical deformation behavior as expected in the case of Mg that has hcp crystal structure deforming mostly along the basal planes and formation of large plateau due to energy absorption indicating twinning activities before failure.[23,24] Similar behavior was observed by several authors,[25–27] and it is connected with mechanical twinning.[28] A pole mechanism for twin formation was proposed by Thompson and Millard,[29] who suggested the following dislocation reaction to form a pole source of twinning:

$$[0\,0\,0\,1] \rightarrow +\alpha[10\bar{1}1] + [1\,0\bar{1}0] \qquad [4]$$

where α is a small fraction, ranging from 1/12 to 1/4. It should be noted that a dislocation with Burgers vector [0 0 0 1] is rigid; therefore, these dislocations are responsible for strain hardening in hcp materials.[30]

Addition of 6.5 wt pct Zn and 10 wt pct HA into pure Mg increased the internal strain of Mg crystallite (*i.e.*, 0.52 and 0.73 pct, respectively). The increment of internal strain could be explained by high generation of internal energy during milling, which triggered the cumulative processing temperature. During mechanical milling, the powder particles were also subjected to high-energy collisions, causing a severe plastic deformation and occurrence of stress yields, which were associated with multiplication of the linear dislocations and refinement of the grains.[31] This situation considerably increased internal strain in the Mg grains, especially with the presence of binary (Zn) and ternary (HA) phases. An increase in internal strain, thus, increased the compressive modulus of the biodegradable Mg-based

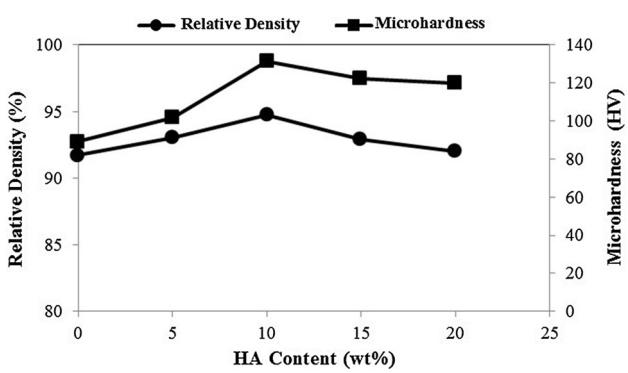

Fig. 5—Relative density and microhardness of pure Mg, Mg-Zn alloy, and Mg-Zn/HA composite.

Table III. Characteristic Compressive Profile of Mg-Zn Alloy and Mg-Zn/HA Composite

HA Content (Wt Pct)	Elastic Modulus (GPa)	Compressive Strength (MPa)	Failure Strain
0	47.4 ± 0.8	249 ± 3	1.36
5	47.8 ± 1.0	265 ± 6	1.13
10	48.4 ± 0.7	292 ± 4	1.08
15	48.1 ± 0.7	281 ± 3	0.71
20	47.2 ± 0.9	267 ± 4	0.52

Table IV. Profile of Corrosion Behavior of Pure Mg, Mg-Zn Alloy, and Mg-Zn/HA Composite

HA Content (Wt Pct)	Corrosion Potential, E_{corr} (V)	Corrosion Current Density, I_{corr} (A cm^{-2})	Polarization Resistance, R_p (Ω)	Degradation Rate ($\times 10^{-2}$ mm/year)
Pure Mg	−1.70 ± 0.2	3.18×10^{-4}	129 ± 2	37.66 ± 0.4
0	−1.50 ± 0.2	5.07×10^{-5}	706 ± 3	5.34 ± 0.8
5	−1.50 ± 0.3	2.67×10^{-5}	911 ± 2	4.20 ± 0.3
10	−1.46 ± 0.1	8.31×10^{-6}	1371 ± 4	3.22 ± 0.6
15	−1.49 ± 0.2	3.42×10^{-5}	881 ± 5	5.17 ± 0.2
20	−1.51 ± 0.1	5.23×10^{-4}	678 ± 3	15.33 ± 0.7

biomaterials. In addition, Table V displays the dislocation density within the crystallites increased with the incorporation of Zn and HA particles. The highest dislocation density was 18.94×10^{-16} m^{-2}, achieved by the dispersion of HA phase and followed by 12.66×10^{-16} m^{-2} with the presence of Zn as the alloying element. The increase in dislocation density resulted in an increase in compressive modulus due to the increase in accumulative defect, which then mutually blocked the dislocation movement of each other when the external pressure was exerted.

From the compressive curve, the plastic region Mg was shortened with the addition of Zn. This situation suggested the hardening onset appeared at a certain lower strain than the curve of pure Mg.[32,33] In most cases, the presence of secondary phase needs to be avoided due to its different properties, which inhibit the dislocation recovery and increase dislocation density, thus contributing to the reduction of elongation.[9] As shown in Figure 6, the ultimate compressive strength of pure Mg (178 MPa) was improved to 249 MPa with the existence of Zn in the Mg matrix. Above the yield, the strain-hardening rate increased until failure. By incorporating HA into the Mg-Zn alloy, the highest ultimate compressive strength of 292 MPa was attained. However, the Mg-Zn/HA composite exhibited a compressive curve without evidence of the softening effect, where the strain hardening rate rapidly increased after yield in a diminutive plastic region. This occurrence indicated that the intrinsic ductility of Mg was mostly reduced by incorporating HA into the matrix, resulting in the low failure strain.[34]

In addition, according to the Hall–Petch law, the relationship between the mechanical strength and crystallite size can be described as

$$\sigma_s = \sigma_0 + kd^{-1/2} \quad [5]$$

where σ_0 and k are constants, d is the crystallite size, and the value of k reflects the sensitivity of the strength to the crystallite size.[35] Therefore, the finer the crystallite, the higher the strength of Mg or Mg-based alloy or Mg matrix composite. The initial crystallite size of pure Mg (194 nm) refined to 21 and 12 nm for the Mg-Zn alloy and Mg-Zn/HA composite, respectively. The crystallite refinement of the studied materials was in agreement with the increment of the compressive strength.

G. *Biodegradation Behavior of Pure Mg, Mg-Zn Alloy, and Mg-Zn/HA Composite*

In this study, Zn and HA were selected as an alloying element and reinforcement phase due to their ability to improve mechanical and corrosion resistance properties. The Mg corrosion in an aqueous environment is given by the following overall reaction:

$$Mg + 2H_2 \rightarrow Mg(OH)_2 + H_2 \quad [6]$$

According to the overall reaction, one molecule of hydrogen (H) is evolved for each atom of corroded Mg. It is possible to determine the weight loss rate of Mg from the volume rate of H_2 released during the corrosion experiment. The occurrence of Mg corrosion increased the pH of the solution due to the reduction of H^+ as a result of the H_2 release.[36,37] The polarization curves for various sintered compacts are given in Figure 7. The electrochemical parameters, including corrosion potential (E_{corr}), corrosion current density (I_{corr}), and polarization resistance (R_p), obtained from the polarization curves by the Tafel extrapolation method and electrochemical impedance spectroscopy studies are listed in Table IV.

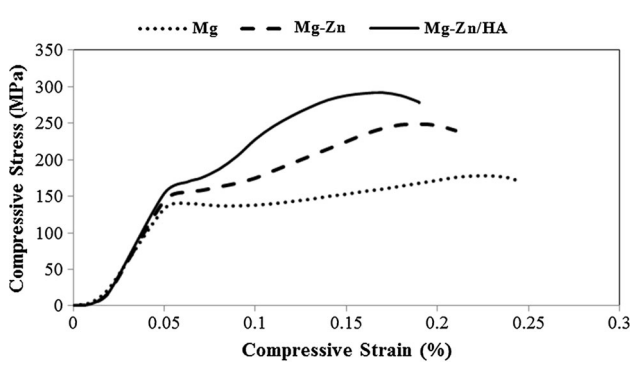

Fig. 6—Compressive stress strain curves of pure Mg, Mg-Zn alloy, and Mg-Zn/HA composite.

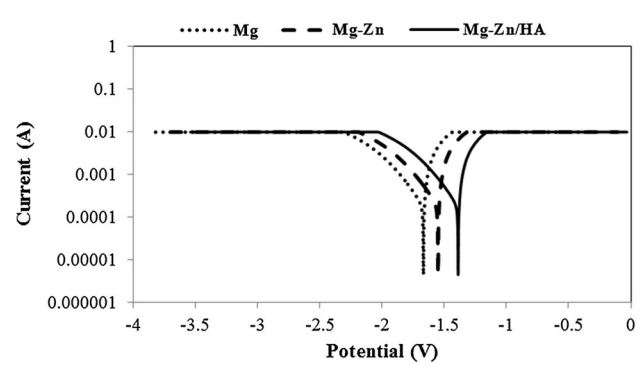

Fig. 7—Linear polarization curves of pure Mg, Mg-Zn alloy, and Mg-Zn/HA composite.

Table V. Profile of Internal Defect of Pure Mg, Mg-Zn Alloy, and Mg-Zn/HA Composite

Specimen	Crystallite Size (nm)	Internal Strain (Pct)	Dislocation Density (10^{-16}) (m^{-2})
Pure Mg	194	0.17	2.66
Mg-Zn Alloy	21	0.52	12.66
Mg-Zn/HA Composite	12	0.73	18.94

The corrosion potentials of the Mg-Zn alloy and Mg-Zn/HA composite were −1.50 and −1.46 V, respectively. Tafel polarization shows that the corrosion potential of both compacts shifted significantly toward the nobler position (positively) than the pure Mg of −1.70 V. These results indicated that the corrosion resistance of Mg was improved by adding Zn as an alloying element, and further enhancement was attained by incorporating the alloy with bioactive HA particles, indicating that the Mg-Zn/HA composite is least susceptible to corrosion followed by Mg-Zn the alloy. The improved corrosion resistance would effectively reduce the initial corrosion rate of metallic implants and greatly sustain the mechanical integrities of the implants in the pretissue or prebone recovery.[38]

A plateau at both cathodic and anodic regions was observed in all polarization curves, indicating the passive layer corresponding to the oxides or any precipitate formed on the exposed surface when the compacts were immersed in the HBSS. It is accepted that the corrosion resistance was relatively dependent on the crystallite size corresponding to grain boundary defects.[39] The crystallite size of pure Mg (194 nm) reduced to 22 and 12 nm of Mg-Zn alloy and Mg-Zn/HA composite, correspondingly. The smaller the crystallite size, the faster the development of the protective layer, which is facilitated by the existence of nucleation sites associated with the defects present in the grain boundaries. The integrity of the protective layer is retained during growth and acts as a barrier for ions coming from the solution and favors corrosion resistance.[40,41] However, once the layer failure is initiated, the cracks increase the OH^- ion diffusivity across the layer and accelerate the corrosion rate.

To account for the corrosion behavior of pure Mg, Mg-Zn alloy, and Mg-Zn/HA composite in HBSS, a Nyquist plot with the high-frequency part of impedance data was measured, as shown in Figure 8. In the Nyquist plots, the capacitive loop of the pure Mg compact is obviously enlarged with the addition of Zn and HA particles. Usually, the capacitive loops are attributed to charge transfer, film effects, and mass transfer in the corrosion product layer.[42] Enlargement of the capacitive loop diameter indicates an increase in impedance and decrease in corrosion rate. The impedances of the Mg-Zn alloy and Mg-Zn/HA composite are 2534 and 1878 Ωcm^2, respectively, which are larger than those of the pure Mg compact (1227 Ωcm^2). The higher impedances indicate the inability of electrolyte ions to penetrate the exposed surface, resulting in lowering the corrosion activity.[43] As can be seen from all samples, there is only a single capacitive semicircle, indicating one time constant and that the film consists of a single dominant corrosion layer.

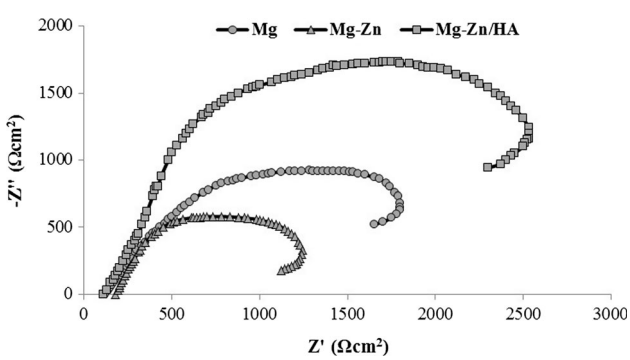

Fig. 8—Nyquist plots for the pure Mg, Mg-Zn alloy, and Mg-Zn/HA composite immersed in HBSS.

During immersion in HBSS, Mg is first oxidized electrochemically to intermediate species Mg^+; then the intermediate species reacts chemically with water to produce H and Mg^{2+}. The presence of Cl^- ions (from HBSS) increases the exposed free area and accelerates the electrochemical reaction rate from Mg metal to Mg^+.[44] The capacitive semicircle is attributed to the redox Mg-Mg^+ reaction, since it was assumed to be the rate-determining step in the charge transfer process. Therefore, the resistance value obtained from intercepts of the capacitive semicircle with real axis corresponds to the charge transfer resistance. The curve manifested that the addition of Zn as an alloying element in the Mg-Zn alloy and HA as a reinforcement in the Mg-Zn/HA composite leads to an increase in the size of the capacitive semicircles, indicating an increase in the resistance and a decrease in the corrosion rate. In the case of Mg-Zn/HA composite, an increase in resistivity arises from the change in chemical composition of the surface deposit due to the incorporation of calcium (Ca) and phosphorus (P) ions into the Mg-Zn matrix, especially through defect sites with low ionic resistance, suggesting that Mg-containing phosphate precipitate on the surface layer significantly reduces the biodegradation of Mg. The polarization and impedance characteristics revealed that biodegradation of Mg is improved with the incorporation of Zn and HA particles.

Figure 9 illustrates the surface morphology of pure Mg, Mg-Zn alloy, and Mg-Zn/HA composite after the immersion effect. The SEM micrographs show that the surfaces of pure Mg and Mg-Zn alloy were completely covered by a number of cracks of corrosion products. The cracks were mostly due to water loss as the specimens were removed from the solution.[9] The high

Table VI. EDX Profile of Pure Mg, Mg-Zn Alloy, and Mg-Zn/HA Composite after Immersion in HBSS

	Element (At. Pct)					
Specimen	O	Na	Zn	Mg	P	Ca
Pure Mg	41.53	3.65	—	54.82	—	—
Mg-Zn Alloy	43.58	3.28	1.28	49.17	—	—
Mg-Zn/HA Composite	47.82	2.32	0.71	42.43	5.24	1.48

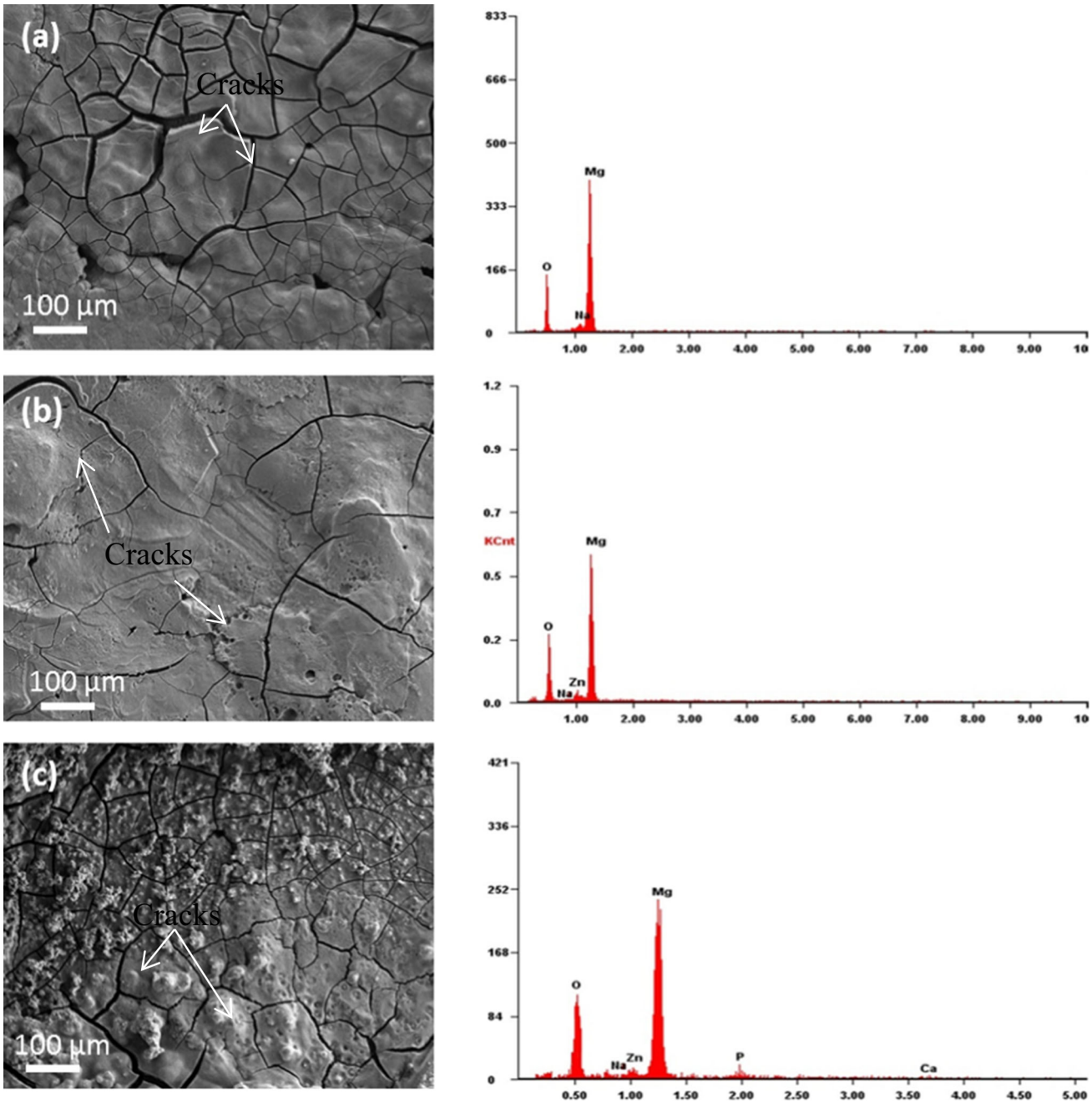

Fig. 9—Microstructure and EDX profile of (*a*) pure Mg, (*b*) Mg-Zn alloy, and (*c*) Mg-Zn/HA composite after the immersion test.

number of cracks on the pure Mg surface reduced as Zn was added, but the cracks grew in size. In the case of Mg-Zn/HA composite, some tiny cracks appeared on the film surface with the presence of some spherical-like structure on top.

Table V lists the chemical compositions of general corrosion products formed on the surface after electrochemical test in a solution that had ion concentrations relevant to human plasma. The results indicated that this layer was mainly composed of oxygen (O), Zn, Mg, P, sodium (Na), and Ca. A high Mg content was found in this layer. The detection of Mg and O corresponded to brucite, which acts as a protective layer. A low fraction of Ca and P that could not be identified in XRD spectra was detected from EDX analysis on the Mg-Zn/HA composite, suggesting the initial formation of Mg-containing phosphate precipitated after the immersion test. However, since the atomic weights of Ca (1.48 at. pct) and P (5.24 at. pct) were considerably low with a Ca:P ratio of 0.28:1, it can be said that the apatite compound was incapable of forming within the duration of immersion test (Table VI).

The formation of this Mg-containing phosphate precipitate was expected to protect the Mg from fast degradation.

Therefore, a plateau was observed on the polarization curves due to the formation of a protective layer of brucite and Mg-containing phosphate.[45] This finding suggested that the protective layer with a low precipitation (in the case of Mg-Zn/HA composite) grew on the exposed surfaces in the simulated body fluid. For all tested sintered compacts, there was no indication of pitting corrosion, as no existence of a hole was observed. In addition, according to the polarization curves, there was no rough appearance of the anodic curve, explaining the lack of associated repeated breakdown and regeneration of the passivation layer in regard to pitting corrosion.[18,42]

IV. SUMMARY AND CONCLUSIONS

Mg-Zn alloy and Mg-Zn/HA composites containing 5, 10, 15, and 20 wt pct HA were fabricated using a powder metallurgy route and sequential consolidation. The microhardness of Mg-Zn alloy reinforced with 5 to 10 wt pct HA increased from 101 to 131 HV, and the relative density reached as high as 94.77 pct. By reinforcing the Mg-Zn alloy with HA particles, the highest compressive strength of 292 MPa was attained at 10 wt pct HA. The corrosion potential (E_{corr}) Mg-Zn/HA composite was −1.46 V, which shifted significantly more toward the passive position than the plain Mg-Zn alloy −1.50 V. These results indicated that the corrosion resistance of Mg-Zn alloy was improved by reinforcing the alloy with bioactive HA particles.

ACKNOWLEDGMENTS

The authors thank the Universiti Sains Malaysia RU-PRGS (Grant No. 8046026) and the Ministry of Higher Education (FRGS Grant No. 6071304) for the financial support and fellowship scheme.

REFERENCES

1. S. Nag, R. Banerjee, and H.L. Fraser: *Acta Biomater.*, 2007, vol. 3, pp. 369–76.
2. M.P. Laura, L. Rink, and H. Haase: *Int. J. Environ. Res. Public Health*, 2010, vol. 7, pp. 1342–65.
3. W. Li, S. Guan, J. Chen, J. Hu, S. Chen, L. Wang, and S. Zhu: *Mater. Charact.*, 2011, vol. 62, pp. 1158–65.
4. M.K. Datta, D.T. Chou, D. Hong, P. Saha, S.J. Chung, B. Lee, A. Sirinterlikci, M. Ramanathan, A. Roy, and P.N. Kumta: *Mater. Sci. Eng. B*, 2011, vol. 176, pp. 1637–43.
5. S. Zhang, X. Zhang, C. Zhao, J. Li, Y. Song, C. Xie, H. Tao, Y. Zhang, Y. He, Y. Jiang, and Y. Bian: *Acta Biomater.*, 2010, vol. 6, pp. 626–40.
6. E.M. Salleh, S. Ramakrishnan, and H. Zuhailawati: *Procedia Chem.*, 2016, vol. 19, pp. 525–30.
7. H. Bahman and A. Abdollah: *J. Alloys Compd.*, 2014, vol. 607, pp. 1–10.
8. H.R. Bakhsheshi-Rad, M.H. Idris, M.R. Abdul-Kadir, A. Ourdjini, M. Medraj, M. Daroonparvar, and E. Hamzah: *Mater. Des.*, 2014, vol. 53, pp. 283–92.
9. F. Witte, V. Kaese, H. Haferkamp, E. Switzer, A.M. Lindenberg, C.J. Wirth, and H. Windhagen: *Biomaterials*, 2005, vol. 26, pp. 3557–63.
10. M. Gupta and N.M.L. Sharon: *Magnesium, Magnesium Alloys, and Magnesium Composites*, 3rd ed., John Wiley and Sons, New York, NY, 2011, pp. 32–67.
11. E.M. Salleh, H. Zuhailawati, S. Ramakrishnan, and M.A.H. Gepreel: *J. Alloys Compd.*, 2015, vol. 644, pp. 476–84.
12. B. Yan and G. Li: *Composites Part A*, 2005, vol. 36, pp. 1590–94.
13. S.Z. Khalajabadi, M.R.A. Kadir, S. Izman, H.R. Bakhsheshi-Rad, and S. Farahany: *Ceram. Int.*, 2014, vol. 40, pp. 16743–59.
14. A. Ruys, A. Brandwood, B. Milthorpe, M. Dickson, K. Zeigler, and C. Sorrell: *J. Mater. Sci., Mater. Med.*, 1995, vol. 6, pp. 297–301.
15. G. Muralithran and S. Ramesh: *Ceram. Int.*, 2000, vol. 26, pp. 221–30.
16. E.M. Salleh, S. Ramakrishnan, and H. Zuhailawati: *Adv. Mater. Res.*, vol. 1133, pp. 75-79.
17. A. Atrens, M. Liu, and N.I.Z. Abidin: *Mater. Sci. Eng. B*, 2011, vol. 176, pp. 1609–36.
18. T. Lei, W. Tang, S.H. Cai, F.F. Feng, and N.F. Li: *Corros. Sci.*, 2012, vol. 54, pp. 270–77.
19. J. Chen, Z. Chen, H. Yan, and F. Zhang: *J. Alloys Compd.*, 2009, vol. 467, pp. 1–7.
20. F. Neves, F.M. Braz Fernandes, I. Martins, and J.B. Correia: *J. Alloys Compd.*, 2011, vol. 509, pp. 271–74.
21. S.R. Agnew, C.N. Tome, D.W. Brown, T.M. Holden, and S.C. Vogel: *Scripta Mater.*, 2003, vol. 48, pp. 1003–08.
22. F. Witte, F. Feyerabend, P. Maier, J. Fischer, M. Stormer, C. Blawert, W. Dietzel, and N. Hort: *Biomaterials*, 2007, vol. 28, pp. 2163–74.
23. P. Klimanek and A. Potzsch: *Mater. Sci. Eng. A*, 2002, vol. 324, pp. 145–50.
24. M.R. Barnett, Z. Keshavarz, A.G. Beer, and D. Atwell: *Acta Mater.*, 2004, vol. 52, pp. 5093–5103.
25. L. Jiang, J.J. Jonas, A.A. Luo, A.K. Sachdev, and S. Godet: *Mater. Sci. Eng. A,* 2007, vols. 445–446, pp. 302–309.
26. Y.N. Wang and J.C. Huang: *Acta Mater.*, 2007, vol. 55, pp. 897–905.
27. N. Dixit, K.Y. Xie, K.J. Hemkera, and K.T. Rames: *Acta Mater.*, 2015, vol. 87, pp. 56–67.
28. N. Thompson and D.J. Millard: *Lond. Edinb. Dublin Philos. Mag.*, 1952, vol. 7, pp. 422–40.
29. H.Q. Sun, Y.N. Shi, M.X. Zhang, and K. Lu: *Acta Mater.*, 2007, vol. 55, pp. 975–82.
30. G. Proust, C.N. Tome, A. Jain, and S.R. Agnew: *Int. J. Plasticity*, 2009, vol. 25, pp. 861–80.
31. A. Blake and C. Caceres: *Mater. Sci. Eng. A*, 2008, vol. 483, pp. 161–63.
32. C. Castellani, R.A. Lindtner, P. Hausbrandt, E. Tschegg, S.E. Stanzl-Tschegg, G. Zanoni, S. Beck, and A.M. Weinberg: *Acta Biomater.*, 2011, vol. 7, pp. 432–40.
33. E. Fidancevska, G. Ruseska, J. Bossert, Y.M. Lin, and A.R. Boccaccini: *Mater. Chem. Phys.*, 2007, vol. 103, pp. 95–100.
34. N. Hort, Y. Huang, D. Fechner, M. Stormer, C. Blawert, F. Witte, C. Vogt, H. Drucker, R. Willumeit, and K. Kainer: *Acta Biomater.*, 2010, vol. 6, pp. 1714–25.
35. Y. Jeong and W. Kim: *Corros. Sci.*, 2014, vol. 82, pp. 392–403.
36. S.E. Harandi, M. Mirshahi, S. Koleini, M.H. Idris, H. Jafari, and M.R.A. Kadir: *Mater. Res.*, 2013, vol. 16, pp. 11–18.
37. Y. Wan, G. Xiong, H. Luo, F. He, Y. Huang, and X. Zhou: *Mater. Des.*, 2008, vol. 29, pp. 2034–37.
38. Y. Jang, B. Collins, J. Sankar, and Y. Yun: *Acta Biomater.*, 2013, vol. 9, pp. 8761–70.
39. D. Yin, E. Zhang, and S. Zeng: *Trans. Nonferrous Met. Soc. China*, 2008, vol. 18, pp. 763–68.
40. D. Zander and N.A. Zumdick: *Corros. Sci.*, 2015, vol. 93, pp. 222–33.
41. C. Ou, W. Lu, Z. Zhan, P. Huang, P. Yan, B. Yan, and M. Chen: *Int. J. Electrochem. Sci.*, 2013, vol. 8, pp. 9518–30.
42. A. Gnedenkov, S. Sinebryukhov, D. Mashtalyar, and S. Gnedenkov: *Surf. Coat. Technol.*, 2013, vol. 225, pp. 112–18.
43. G.L. Song: *Corros. Sci.*, 2007, vol. 49, pp. 1696–1701.